Cancer-Associated Fibroblasts Promote Immunosuppression by Inducing ROS-Generating Monocytic MDSCs in Lung Squamous Cell Carcinoma

Handan Xiang[1], Carlo P. Ramil[2], Josephine Hai[3], Chunsheng Zhang[4], Huijun Wang[5], Amanda A. Watkins[1], Roshi Afshar[1], Peter Georgiev[1], Marc A. Sze[4], Xuelei S. Song[3], Patrick J. Curran[3], Mangeng Cheng[3], J. Richard Miller[3], Dongyu Sun[3], Andrey Loboda[4], Yanlin Jia[1], Lily Y. Moy[3], An Chi[2], and Philip E. Brandish[1]

ABSTRACT

Cancer-associated fibroblasts (CAF) represent a functionally heterogeneous population of activated fibroblasts that constitutes a major component of tumor stroma. Although CAFs have been shown to promote tumor growth and mediate resistance to chemotherapy, the mechanisms by which they may contribute to immune suppression within the tumor microenvironment (TME) in lung squamous cell carcinoma (LSCC) remain largely unexplored. Here, we identified a positive correlation between CAF and monocytic myeloid cell abundances in 501 primary LSCCs by mining The Cancer Genome Atlas data sets. We further validated this finding in an independent cohort using imaging mass cytometry and found a significant spatial interaction between CAFs and monocytic myeloid cells in the TME. To delineate the interplay between CAFs and monocytic myeloid cells, we used chemotaxis assays to show that LSCC patient–derived CAFs promoted recruitment of $CCR2^+$ monocytes via CCL2, which could be reversed by CCR2 inhibition. Using a three-dimensional culture system, we found that CAFs polarized monocytes to adopt a myeloid-derived suppressor cell (MDSC) phenotype, characterized by robust suppression of autologous $CD8^+$ T-cell proliferation and IFNγ production. We further demonstrated that inhibiting IDO1 and NADPH oxidases, NOX2 and NOX4, restored $CD8^+$ T-cell proliferation by reducing reactive oxygen species (ROS) generation in CAF-induced MDSCs. Taken together, our study highlights a pivotal role of CAFs in regulating monocyte recruitment and differentiation and demonstrated that CCR2 inhibition and ROS scavenging abrogate the CAF–MDSC axis, illuminating a potential therapeutic path to reversing the CAF-mediated immunosuppressive microenvironment.

Introduction

Non–small cell lung cancer (NSCLC) is the leading cause of cancer mortality worldwide and comprised of two major histologic subtypes: lung adenocarcinoma (LADC) and lung squamous cell carcinoma (LSCC). The clinical success of immune-checkpoint inhibition highlights the importance of therapeutically harnessing host antitumor immune responses to eliminate cancer (1). However, only a small subset of patients responds to immune-checkpoint inhibition (1), indicating that additional mechanisms of immune evasion operate within the tumor microenvironment (TME) to further dampen antitumor immune responses. Thus, understanding diverse mechanisms underlying immune suppression is critical for providing new therapeutic avenues or combinatorial strategies for NSCLC treatment.

Cancer-associated fibroblasts (CAF) are activated fibroblasts that have a tremendous influence on remodeling the stromal compartment within the TME through collagen deposition and matrix metalloproteinase secretion (2). Previous studies revealed protumorigenic roles of CAFs in accelerating tumor proliferation, metastasis, and shielding tumors from drug penetrance (2–5). Although CAFs are one of the most abundant cell types in the tumor stroma (6), how CAFs interact with tumor-infiltrating immune cells (TIIC) to shape the immunoevasive TME remains poorly defined. Genomic studies from clinical patient samples have suggested that stromal fibroblasts may mediate resistance to checkpoint inhibitors (7, 8). Thus, understanding the immunosuppressive functions of CAFs can inform novel therapeutic strategies to unleash host antitumor immune responses.

Emerging evidence suggests an important cross-talk between CAFs and immuno-inhibitory cell types, which may be attributed to the immunosuppressive function of CAFs (9–11). One study has reported that $FAP^+PDGFR\beta^+$ CAFs in breast cancer attract $CD4^+CD25^+$ T cells by secretion of CXCL12 and promote $CD4^+$ T-cell differentiation into $FOXP3^{high}$ regulatory T cells by expression of B7H3, CD73, and DPP4 (9), whereas other studies have demonstrated that CAFs contribute to immunosuppressive M2-like TAM induction in breast cancer and oral squamous cell carcinoma (6, 10). Collectively, the existing evidence suggests that CAFs orchestrate immunosuppression by tightly regulating TIICs in the TME, but studies in NSCLC investigating the effects of stromal fibroblasts on modulating TIICs remain limited. In our study, we report a positive correlation between CAF and monocytic myeloid cell accumulation in LSCC. We further dissect this association functionally to formulate a model of how

---

[1]Discovery Oncology, Merck & Co., Inc., Boston, Massachusetts. [2]Chemical Biology, Merck & Co., Inc., Boston, Massachusetts. [3]Pharmacology, Merck & Co., Inc., Boston, Massachusetts. [4]Informatics, Merck & Co., Inc., Boston, Massachusetts. [5]Modeling and Informatics, Merck & Co., Inc., Kenilworth, New Jersey.

Note: Supplementary data for this article are available at Cancer Immunology Research Online (http://cancerimmunolres.aacrjournals.org/).

C.P. Ramil and J. Hai contributed equally to this article.

Current address for P.E. Brandish: Bicycle Therapeutics, Lexington, Massachusetts.

Corresponding Authors: Philip E. Brandish, Bicycle Therapeutics, Lexington, MA 02421. Phone: 484-213-1698; E-mail: phil.brandish@bicycletx.com; and Handan Xiang, Merck & Co., Inc., 33 Avenue Louis Pasteur, Boston, MA 02115. Phone: 617-992-3151; E-mail: handan.xiang@merck.com

Cancer Immunol Res 2020;8:436–50

doi: 10.1158/2326-6066.CIR-19-0507

CAFs induce immunosuppressive monocytic MDSCs to sculpt a permissive TME in NSCLC.

Materials and Methods

Ethics statement

All primary human LSCC samples used in this study were purchased from the Clinical and Translational Science Institute (CTSI) at the University of Minnesota, with patient consent approved by the Institutional Review Board protocol #0305M47681 in accordance with ethical standard of the US Common Rule and the Belmont Report. The CTSI is supported through the NIH, grant UL1TR002494. Human peripheral whole blood was purchased from the HemaCare Corporation with donor's informed consent. Please refer to the "Primary LSCC tissue and human cell lines" section, as well as Supplementary Table S1, for more details.

The Cancer Genome Atlas and published study data set analysis

The Cancer Genome Atlas (TCGA) database for 501 LSCC patient samples and 503 LADC patient samples was used for analysis of clinical relevance. RNA-sequencing data were downloaded from the TCGA portal (https://portal.gdc.cancer.gov/; ref. 12) as of September 2015 (8). The expression data were $\log_{10}$ transformed. Spearman correlation was used to determine the correlation coefficient between indicated gene expression. To compare the expression of *CCL2, IL6*, and *VEGF* in the $\mathrm{FAP}^{\mathrm{high}}$ and $\mathrm{FAP}^{\mathrm{low}}$ groups, LSCC patients were divided into $\mathrm{FAP}^{\mathrm{high}}$ and $\mathrm{FAP}^{\mathrm{low}}$ groups based on the *FAP* median expression value, and the Wilcoxon rank-sum test was used to calculate P value. Statistical analyses and visualizations were performed with Matlab R2010b Version 7.11.2.

To analyze specific gene abundance within the Lambrechts and colleagues study (13), zipped files containing an RDS file were downloaded from https://www.ebi.ac.uk/arrayexpress/experiments/E-MTAB-6149/ on October 2, 2019. The files were unzipped, and the RDS file named "Allsamples.Cellview.Rds" was used to investigate the expression distribution of *CCL2, IL6, CXCL1, CXCL5, CCL7*, and *MIF*. To generate the violin plots, cells that had an *EPCAM* count greater than 0 and *EPCAM* greater than *FAP* or *CD45* were binned as EPCAM^{+} cells. Cells that had a *FAP* count greater than 0 and *FAP* greater than *EPCAM* or *CD45* were binned as FAP^{+} cells. Cells that had a *CD45* count greater than 0 and *CD45* greater than *EPCAM* or *FAP* were binned as $\mathrm{CD45}^{+}$cells. All other cells were binned into an "Other" category. Cutoffs used to determine each cell type were unchanged from the original figure generated from Lambrechts and colleagues (13). All gene-expression data analysis and data visualizations were performed by R Version 3.5.2 and the R package Tidyverse Version 1.2.1.

Primary LSCC tissue and human cell lines

Two cohorts were used in this study: cohort A ($n = 10$) for imaging mass cytometry (IMC) analysis and cohort B ($n = 2$) for isolating primary CAFs (Supplementary Table S1). The two cohorts ($n = 12$) were representative of a population of LSCC patients with a median age of 65.5 years, a high percentage without prior systemic therapy (83%), and all current/former smokers (Supplementary Table S1). Formalin-fixed paraffin-embedded tissue sections were obtained from each patient in the cohort.

Human SW900, H2170, and H520 cells were purchased from the American Type Culture Collection, authenticated by short-tandem repeat profiling and kept in culture for no more than 5 passages. Cell lines were tested for *Mycoplasma*, cultured in RPMI-1640 medium supplemented with 2 mmol/L glutamine (Thermo Fisher Scientific), 10 mmol/L HEPES (Thermo Fisher Scientific), 1X nonessential amino acids (Thermo Fisher Scientific), 1 mmol/L sodium pyruvate (Thermo Fisher Scientific), 10% heat-inactivated FBS (Thermo Fisher Scientific), and maintained at 37°C and 5% CO_2.

LSCC-derived CAF isolation and culture

CAF_01 was purchased from Vitro BioPharma (CAF07-S). CAF_02 and CAF_03 were derived from freshly resected tumor samples purchased from the University of Minnesota, and patient clinicopathologic features are described in the cohort B section of Supplementary Table S1. Lung tumors were minced into $\sim$1 mm^3 fragments, placed in 6-well uncoated culture plates with DMEM supplemented with 10% FBS to allow for CAF cells to extravasate from tissue and expand until cells became confluent before passaging. CAFs from all 3 donors were confirmed by flow cytometry analysis using fibroblast markers: FAP (clone: 427819, R&D Systems), PDGFRβ (clone: 28D4, BD), and CD90 (clone: 5E10, BioLegend). CAFs were used in subsequent experiments within 10 passages from thawing.

IHC and IMC

Tumor samples were fixed in 10% formalin, and then stored in 70% ethanol before processing and embedding. IHC was conducted on 5-μm sections. Twelve tissue sections from the patients in cohorts A and B (Supplementary Table S1) were deparaffinized, rehydrated, and boiled for 15 minutes with DC NxGen (Biocare Medical). Slides were incubated in Peroxidazed 1 (Biocare Medical, PX968) for 5 minutes and then blocked with Background Punisher (Biocare Medical, IP974G20) for 10 minutes before staining with primary antibodies: TTF1 (Abcam, ab133638, 1:2,000 dilution) and P63 (Biocare Medical, CM 163A, 0.5 μg/mL dilution). Lung squamous cell carcinoma was confirmed by histology and p40, p63, and TFF-1 IHC. Tumors were assessed for staining positivity, and no intensity scoring was done.

5-μm tissue sections from cohort A were processed and stained using 17 fibroblast and immune cell markers for IMC as previously described (14). IMC antibodies are listed in Supplementary Table S2. Hyperion Imaging System (Fluidigm) was used to acquire a randomly selected 1 mm × 1 mm tumor area on slides for each LSCC section. IMC data analysis was performed as previously described (14). In brief, IMC imaging mcd. files were exported into tiff files using the Fiji software, which were subsequently used to generate cell segmentation masks by Ilastik Version 1.3.2. Cell segmentation masks were then imported into CellProfiler Version 3.1.5 to extract single-cell staining intensity and generate probability masks (15). Tiff files and the corresponding probability masks were imported into the imaging analyzing software histoCAT Version 1.75 for subsequent analysis (14). Two-dimensional graphs using a multidimensional reduction tool, t-SNE, to project high-dimensional single-cell data into two dimensions were used to visualize and quantify marker-specific cell types (14, 16). An unsupervised clustering algorithm, Phenograph, to define complex phenotypes shared across tumors based on the staining intensity of tested cell markers was used to define cell clusters, which were further used to run neighborhood analysis to reveal significant interactions or avoidances of cell–cell neighbors that were reflective of cellular organization (14). For neighborhood analysis, a permutation test to compare the number of interactions between all cell types in a given image to that of a matched control containing randomized cell phenotypes was used to determine the P value (14). T-SNE plots from each individual LSCC samples were used to quantify percentage of marker-specific cell types. Spearman correlation was used to calculate the correlation between FAP$^+$ fibroblast and immune cell abundancies.

Neutrophil isolation and flow staining

Human peripheral whole blood from NSCLC and colorectal cancer donors was purchased from the vendor HemaCare Corporation. Granulocytes were negatively selected from whole blood using the MACSxpress Whole Blood Neutrophil Isolation Kit (Miltenyi Biotec) according to the manual. Granulocytes were diluted with RPMI-1640 (Thermo Fisher Scientific) and mixed with Ficoll-Paque PLUS (GE Healthcare). Samples were then centrifuged for 20 minutes at 1,200 rpm at room temperature with the brake OFF. Neutrophils were collected from the lower layer of samples. Five microliters of the human Fc blocking solution (BioLegend) and the live/dead dye from the LIVE/DEAD Fixable Near-IR Dead Cell Stain Kit (Thermo Fisher Scientific) were added prior to antibody staining over ice according to the manuals. Antibodies shown in Supplementary Table S3 were used for staining. CXCR1$^+$ or CXCR2$^+$ neutrophils were analyzed as indicated in the "Flow cytometry" section later.

PBMC and CD14$^+$ monocyte isolation

Human peripheral blood leukopaks from 3 independent healthy donors (D108, D878, and D283) were purchased from STEMCELL Technologies. Peripheral blood mononuclear cells (PBMC) were isolated from leukopaks using Lymphoprep (STEMCELL Technologies) via density gradient centrifugation according to the manufacturer's instructions. For CD14$^+$ monocyte isolation, CD14 microbeads (Miltenyi Biotec, catalog number: 130-050-201) were used to positively enrich CD14$^+$ monocytes from PBMCs according to the manual and further verified for CD14 expression using flow cytometry analysis with a purity of >90% CD14$^+$. The anti-CD14$^+$ antibody used here is listed in Supplementary Table S3.

Monocyte differentiation

Isolated CD14$^+$ monocytes were seeded at 2×10^6 per well in an ultra-low attachment 6-well plate (Corning). Immature dendritic cells (iDC) were differentiated using ImmunoCult Dendritic Cell Culture kit (STEMCELL Technologies) for 7 days according to the manufacturer's instructions. Macrophages were differentiated using ImmunoCult-SF Macrophage Media (STEMCELL Technologies) supplemented with M-CSF (50 ng/mL; STEMCELL Technologies) for 1 week. For M1 macrophage differentiation, LPS (10 ng/mL; Sigma-Aldrich) and IFNγ (50 ng/mL; STEMCELL Technologies) were added on day 5; M2 macrophages were polarized by adding IL4 (10 ng/mL; STEMCELL Technologies) on day 5. For cytokine-generated MDSCs, monocytes were cultured in media plus IL6 (20 ng/mL; R&D Systems) and GM-CSF (20 ng/mL; R&D Systems) for a week. For CAF-educated MDSCs, 1 million CAFs were embedded in 50% growth factor–reduced basement membrane extract (BME; R&D Systems) in a transwell with a 0.4-μm pore size to separate them from the monocytes but to allow exchange of growth factors and cytokines. Two million monocytes in the lower chamber were cultured in RPMI-1640 medium supplemented with 2 mmol/L glutamine (Thermo Fisher Scientific), 10 mmol/L HEPES (Thermo Fisher Scientific), 1× nonessential amino acids (Thermo Fisher Scientific), 1 mmol/L sodium pyruvate (Thermo Fisher Scientific), 10% heat-inactivated FBS (Thermo Fisher Scientific), and GM-CSF (20 ng/mL; R&D Systems) for a week. Media supplemented with fresh GM-CSF were changed on day 4. Cells were maintained at 37°C, 5% CO_2.

RNA extraction and RT-qPCR

One million CAF_01 cells were cocultured with 2 million CD14$^+$ monocytes for 7 days as described earlier for generating CAF-educated MDSCs. During the 7-day differentiation phase, the cocultures were untreated or treated with either an IgG isotype control or a neutralizing IL6 antibody (10 μg/mL; BioLegend, clone: MQ2-13A5). At day 7, cells from each group were collected and lysed in lysis buffer RLT (Qiagen, RNeasy Mini Kit). RNAs were extracted from the cell lysates according to the manufacturer's instruction (Qiagen, RNeasy Mini Kit). One microgram RNA from each group was used for reverse transcription according to the manual (Bio-Rad, iScript cDNA Synthesis Kit). TaqMan gene-expression system (Thermo Fisher Scientific) and QuantStudio 6 Flex Real-Time PCR System (Thermo Fisher Scientific) were used to perform RT-qPCR. The following RT-qPCR primers (Thermo Fisher Scientific) were used: *GAPDH* (Hs02786624_g1), *RPL30* (Hs00265497_m1), *RPLP0* (Hs00420895_gH), *RPLP1* (Hs01653088_g1), and *CYBB* (Hs00166163_m1). *GAPDH, RPL30, RPLP0*, and *RPLP1* were used for normalization. The average Ct value ($C_{T\ \mathrm{reference}}$) of *GAPDH, RPL30, RPLP0*, and *RPLP1* (four reference genes) was calculated, and ΔC_T ($C_{T\ \mathrm{treatment}} - C_{T\ \mathrm{reference}}$) was determined. $2^{(-\Delta\Delta CT\ (\Delta CT\ IL6\ -\ \Delta CT\ untreated))}$ and $2^{(-\Delta\Delta CT\ (\Delta CT\ IgG\ -\ \Delta CT\ untreated))}$ were used to calculate the relative fold change of *CYBB* (*NOX2*) in the IgG treatment group versus the IL6-neutralizing antibody treatment group.

Flow cytometry

Cultured human CAFs, tumor cell lines, human monocytes, and *in vitro*–differentiated macrophages, iDCs, and MDSCs were analyzed by flow cytometry using a Fortessa flow cytometer (BD Biosciences). A total of 1×10^5 cells were resuspended in 100 μL of autoMACS Running Buffer (Miltenyi Biotech) for each antibody staining. Five microliters of the human Fc blocking solution (BioLegend) and the live/dead dye from the LIVE/DEAD Fixable Near-IR Dead Cell Stain Kit (Thermo Fisher Scientific) were added prior to antibody staining over ice according to the manuals. For staining chemokine receptors on monocytes, frozen CD14$^+$ monocytes isolated using microbeads were recovered at 37°C for 10 minutes in autoMACS Running Buffer with the addition of the human Fc blocking solution and the LIVE/DEAD fixable dye and stained with indicated antibodies for additional 15 minutes. For ROS measurement, the CellROX Orange Flow Cytometry Assay Kit (Thermo Fisher Scientific) was used, and the experiment was performed according the manual with a few modifications. CAFs were cocultured with monocytes for 6 days as described earlier to generate CAF-induced MDSCs. On day 6, 10 μmol/L NOX inhibitor (obtained from the Merck compound library; ref. 17), 10 μmol/L NOX2 inhibitor (GSK-2795039, MedChem Express #HY-18950; ref. 18), or 1 μmol/L IDO1 inhibitor (Merck & Co., Inc.; ref. 19) were added to cultures for 1 day. On day 7, CAF-induced MDSCs were detached, and the CellROX reagent at 1 μmol/L was added into cell suspension for 1 hour at 37°C in the presence of the NOX inhibitor, NOX2 inhibitor, and IDO1 inhibitor at aforementioned concentrations. A ROS inducer, tert-butyl hydroperoxide (TBHP; Thermo Fisher Scientific) at 400 μmol/L, was used to treat cells for 1 hour as a positive control before adding the CellROX reagent. Flow cytometry antibodies are listed in Supplementary Table S3. Data analysis was performed using FlowJo (Version 10). Cells were first gated based on forward (FSC-A) and side (SSC-A) scatters to exclude debris. Single cells were then selected based on SSC-A versus SSC-W parameters. Dead cells were excluded based on the positive staining of the Live/Dead dye. The positive cell-surface staining of CXCR1, CCR2, and CXCR2 of gated live cells was determined by comparing to fluorescence minus one negative controls. For neutrophil staining, CD3 and CD19 antibodies were first used to gate out the remaining lymphocytes. $CD66^+$ and $CD15^+$ cells were considered as neutrophils. Mean fluorescence intensity (MFI) was used to determine the expression intensity of cell-surface markers, including CD14, CD11b, CD33, DC-SIGN, CD206, CD163, HLA-DR, CD86, and CD16, in monocyte-derived cells.

Cytokine and chemokine quantification assay

For quantifying chemokines, cytokines, and growth factors secreted by CAFs, 1.5 million CAFs were embedded in 600 uL of 50% growth factor-reduced BME (R&D Systems) diluted in RPMI-1640 media in a transwell with a 0.4-μm pore size with 2 mL RPMI-1640 media in the lower chamber. RPMI-1640 medium is supplemented with 2 mmol/L glutamine (Thermo Fisher Scientific), 10 mmol/L HEPES (Thermo Fisher Scientific), 1× nonessential amino acids (Thermo Fisher Scientific), 1 mmol/L sodium pyruvate (Thermo Fisher Scientific), 10% heat-inactivated FBS (Thermo Fisher Scientific). After 3 days, media in the lower chamber were collected and analyzed using the V-PLEX Proinflammatory Panel 1 Human Kit, a customized GM-CSF and VEGF kit, and the U-plex chemokine combo1 and combo2 kits (Meso Scale Discovery) according to the manufacturer's instructions and measured by a SECTOR Imager S 600 (Meso Scale Discovery). Calibrator blends provided in kits are added and analyzed together with samples in the same plates. DISCOVERY WORKBENCH software (Meso Scale Discovery) was used to calculate sample concentrations. The concentrations of calibrator blends and raw values obtained after reading plates were used to generate standard curves to calculate concentrations of secreted factors in conditioned media.

Chemotaxis assay

The IncuCyte ClearView 96-well migration plate (Essen BioScience) was used to perform the chemotaxis assay according to the manufacturer's instruction. In brief, freshly isolated monocytes using CD14 microbeads (Miltenyi Biotec) were loaded into the insert well at a cell density of 5,000 cells/well. For chemotactic migration of monocytes, 200 μL of supernatants from CAFs was added into reservoir wells. For chemokine-induced migration, IL8 (PeproTech), CXCL1 (PeproTech), CCL2 (PeproTech), CCL7 (PeproTech), and CXCL5 (PeproTech) were reconstituted in PBS. CCL2 (5, 10, 20 ng/mL), CCL7 (2, 4, 8 ng/mL), CXCL8 (2, 10, 50 ng/mL), CXCL1 (3.3, 10, 30 ng/mL), and CXCL5 (5, 10, 20 ng/mL) in the complete RPMI-1640 medium were added into wells of reservoir plates to attract monocytes. The complete RPMI-1640 medium is the same one for culturing CAF-induced MDSCs. The CCR2 inhibitor (Santa Cruz, catalog number: sc-202525) was reconstituted in DMSO. Cells were incubated with 0.25 or 0.5 μmol/L CCR2 inhibitor for 30 minutes in insert plates before putting on top of reservoir plates. Insert plates and reservoir plates were incubated for 1.5 hours to facilitate monocyte migration. For data quantification, whole-well images of cells on the bottom and the top of the insert membrane were captured by IncuCyte ZOOM instrument (Sartorius) at 10× magnification. All images were processed using IncuCyte Chemotaxis Software (Sartorius) and the Chemotaxis Migration (Top/Bot) analysis job type to quantify cell areas on each side of the membrane. Directed cell migration was reported as normalized total area (lower side cell area normalized to initial upper side cell area). Three individual wells were used for each group.

$CD8^+$ T-cell suppression assay

Autologous T cells were isolated from the same PBMC donors (D108, D878, and D283) using the EasySep Human $CD8^+$ T-cell isolation kit (STEMCELL Technologies). $CD8^+$ T cells were labeled with 10 μmol/L CFSE (BD Biosciences) in PBS with 0.1% BSA at 37°C for 10 minutes. CAF-induced MDSCs were detached from plates by using Detachin (Genlantis). $CD8^+$ T cells (1×10^5) were cultured with CAF-induced MDSCs at a 1:1 or 2:1 ratio in an untreated sterile U-bottom 96-well plate. $CD8^+$ T cells were stimulated with IL2 (100 U/mL; Thermo Fisher Scientific) and CD3/CD28 dynabeads (Thermo Fisher Scientific) at a 1:1 bead:T cell ratio. To evaluate the impact of the IDO1, NOX, NOX2 inhibitors, tryptophan or N-acetylcysteine on reversing the inhibition of T-cell proliferation by CAF-induced MDSCs, the IDO1 inhibitor (0.3, 1, 3 μmol/L), 10 μmol/L NOX inhibitor, 10 μmol/L NOX2 inhibitor, 25 μmol/L tryptophan (Sigma) or N-acetylcysteine (Thermo Fisher Scientific) at 0.5, 2, 5 mmol/L were added into cocultures for 3 days. To assess the impact of kynurenine on $CD8^+$ T-cell proliferation, 1×10^5 CFSE-labeled $CD8^+$ T cells were stimulated with IL2 (100 U/mL; Thermo Fisher Scientific) and CD3/CD28 dynabeads (Thermo Fisher Scientific) at a 1:1 bead:T-cell ratio, and kynurenine (Sigma; at 2.5, 5, 15, 30, 100, or 300 μmol/L) was incubated in cultures for 3 days. After 3 days, T-cell proliferation was assessed by CFSE dilution using a Fortessa flow cytometer (BD Biosciences), and supernatants were collected for analysis of IFNγ production using the Human IFNγ Tissue Culture Kit (Meso Scale Discovery). The FlowJo Version 10 was used to calculate the MFI of CFSE in cells. The percentage of suppression was calculated using the established formula (20): $((\mathrm{Log2}(y)$ of Teff alone – $\mathrm{Log2}(y)$ of Teff + myeloid cells) / $\mathrm{Log2}(y)$ of Teff alone) × 100, where y is the MFI of CFSE on the whole population divided by the MFI of CFSE of nonproliferating cells.

Western blot

CAFs and CAF-induced MDSCs grown in cultures were detached from plates using Detachin (Genlantis), and cell pellets were washed once using cold PBS. Cells were lysed by using the 1× Cell Lysis Buffer (10× Cell Lysis Buffer, Cell Signaling Technology) supplemented with 1 mmol/L PMSF (Cell Signaling Technology) and 1× protease inhibitor cocktail (100× Halt Protease Inhibitor Cocktail, Thermo Fisher Scientific) and incubated over ice for 30 minutes. Cell lysates were then spun at 14,000 × g in a cold microfuge for 10 minutes. Supernatants were removed, and protein concentrations were determined by the BCA assay according to the manual (Thermo Fisher Scientific). Proteins (25 μg) of each protein sample were loaded onto the NuPAGE 4%–12% Bis-Tris Gel (Thermo Fisher Scientific) and transferred using the Trans-Blot Turbo Transfer Pack according to the manual (Bio-Rad). Blots were incubated with anti-NOX4 (clone: UOTR1B493, Abcam, 1:1,000) or anti-β-actin (clone: AC-15, Sigma, 1:25,000) overnight in a cold room and then stained with HRP-linked secondary antibodies (Cell Signaling Technology, 1:2,000) for 1 hour at room temperature. Blots were then scanned by ChemiDoc imaging system (Bio-Rad).

Kynurenine quantification

LC/MS/MS analyses were performed using the LX4-TSQ Quantum Ultra system (Thermo Fisher Scientific) per the manufacturer's recommendation. This system consists of four Agilent binary high-performance liquid chromatography (HPLC) pumps and a TSQ Quantum Ultra triple quadrupole MS/MS instrument. For each sample, 5 μL was injected onto an Atlantis T3 column (Waters). The mobile phase gradient pumped at 0.8 mL/min was used to elute the analytes from the column at 25°C. Mobile phase A consisted of 0.1% formic acid in water. Mobile phase B consisted of 0.1% of formic acid in acetonitrile. Data were acquired in positive mode using a HESI interface. The operational parameters for the TSQ Quantum Ultra instrument were a spray voltage of 4,000 V, capillary temperature of 380°C, vaporizer temperature 400°C, sheath gas 60 arbitrary units, Aux gas 20 arbitrary units, tube lens 85, and collision gas 1.2 mTorr. SRM chromatograms of kynurenine and internal standard were collected for 90 seconds. The peak area was integrated by Xcalibur Quan software (Thermo Fisher Scientific). The ratios between the kynurenine generated in the reaction and 2D6-Kynurenine spiked-in internal standard were used to quantify kynurenine concentrations.

Proteomics

One million cells each of CAF-educated MDSCs and iDCs from three biological replicates were processed using the iST sample preparation kit (PreOmics). Resulting peptides were resuspended to a final concentration of 1 μg/mL based on the measured total protein amount using a BCA protein assay kit (Thermo Fisher Scientific). Mass spectrometry analyses were performed in Q Exactive HF hybrid quadrupole-orbitrap mass spectrometer (Thermo Fisher Scientific). A 10-μL solution of peptides was separated on a 75-cm C18 EASY-Spray LC column (Thermo Fisher Scientific) heated at 55°C using a 5-hour gradient of 3% to 40% acetonitrile in water with 0.1% formic acid. The instrument was operated in data-dependent mode with a survey scan range of 300 to 1650 m/z and a resolution of 60,000. The RAW MS files were processed using MaxQuant (Version 1.6.0.13) and searched against human sequences from the Uniprot-Swiss-prot database (Uniprot; release 2015-02; 89,796 entries). Default settings within MaxQuant were used with the additional option match between runs. The MaxQuant protein intensity outputs were further processed using Perseus (Version 1.6.0.7). Protein intensities were normalized across samples using the median value to correct for batch effects. Missing values were imputed after filtering for valid values ($n = 3$) in at least one group, and a Student t test was used to compare the two groups to identify significant differentially expressed proteins. The proteins with P-value less than 0.05 and Log2 fold change greater than 1.0 are annotated as significant. All the significant proteins are reviewed with the original intensity readout. Proteins significantly upregulated in either CAF-induced MDSCs or iDCs were used to run pathway enrichment analysis using MetaCore (Clarivate Analytics, https://portal.genego.com/). Several enriched pathways were selected to demonstrate the difference between CAF-induced MDSCs and iDCs with P value listed by MetaCore.

Superoxide anion detection

CAF-induced MDSCs were generated as described above. On day 6, these cells were treated with DMSO or the NOX2 inhibitor at 1 μmol/L or 10 μmol/L for a day. On day 7, cells were detached for superoxide anion measurement by using a Superoxide Anion Assay Kit (Sigma-Aldrich). Cells from control or treatment groups were resuspended in the Assay Medium from the kit to a concentration of 2×10^5 cells/100 μL, and the remaining kit components were added into a Nunc-Immuno MicroWell 96-well polystyrene white plate according to the manufacturer's protocol. DMSO or the NOX2 inhibitor at 1 or 10 μmol/L was subsequently added into the control or treatment group. The luminescence intensity was measured using Envision multilabel reader (PerkinElmer).

Statistical analysis

Statistical analysis was performed using GraphPad Prism 6 (GraphPad software). Statistical tests applied are indicated in the legends or corresponding method sections. Differences were considered statistically significant when $P \leq 0.05$.

Results

A positive correlation between FAP$^+$ CAFs and monocyte abundances is identified in primary LSCC

We first sought to understand whether CAFs were associated with TIICs in the TME by mining the publicly available TCGA cohorts involving 501 LSCC and 503 LADC patients. We measured correlations between fibroblast activation protein (FAP), a widely used marker for CAFs (4, 21), and several TIIC markers. These markers included monocytic myeloid cell markers (CD14, CD33, CD16a), a granulocytic myeloid cell marker (CD66b), T-cell markers (CD8a, CD4), and B-cell markers (CD20, CD19). Among all TIL lineage markers, we found that the expression of FAP and CD14, CD33, and CD16a were correlated. LSCC exhibited a higher correlation between the expression of FAP and CD14, CD33, and CD16a than LADC ($r =$ 0.59, 0.46, 0.52 in LSCC vs. $r =$ 0.34, 0.30, 0.43 in LADC, respectively; **Fig. 1A**; Supplementary Fig. S1). Additional fibroblast markers, including CD90 and PDGFRβ, also showed positive correlations with monocytic myeloid cell markers in LSCC, but not in adjacent nonmalignant lung tissues (Supplementary Figs. S2 and S3). Thus, we decided to focus on LSCCs to further explore the relationship between CAFs and monocytic myeloid cells.

We next used IMC on an independent cohort of 10 primary LSCCs to validate the correlation seen in the TCGA cohort and understand the spatial distribution of the FAP$^+$ and monocytic cell populations. We multiplexed 17 fibroblast and immune cell markers on histologically confirmed LSCC samples (**Fig. 1B–D**; Supplementary Fig. S4A). A cell segmentation mask is shown in **Fig. 1E**, and t-SNE plots were generated from 10 samples to visualize marker-specific cell types (**Fig. 1F**; Supplementary Fig. S4B) by using histoCAT software. We found that a percentage of FAP$^+$ cells positively correlated with CD14$^+$ monocytic myeloid cells but not with CD8A$^+$ T cells or CD20$^+$ B cells in this cohort of LSCCs ($P = 0.0268$; **Fig. 1G**; Supplementary Fig. S5).

Because the program histoCAT enables spatial interrogation of cell–cell interactions, we further used Phenograph analysis and identified 21 phenotype clusters shared across all samples (ref. 22; **Fig. 1H**). These cell phenotypes are characterized by specific epitopes. We showed that clusters 5, 6, and 12 contained cells with high FAP expression and additional canonical fibroblast markers, such as a-SMA, collagen I, and CD90, indicative of a CAF identity (23, 24). Cluster 4 consisted of a cell population expressing a combination of the markers, CD14, CD16 and CD33, which is suggestive of monocytic identity. We subsequently performed neighborhood analysis to reveal significant interactions or avoidances of cell–cell neighbors that are reflective of cellular organization (14). We found that in 70% of tested samples, cluster 5 (CAFs) significantly interacted with cluster 4 (monocytic myeloid cells; $P < 0.01$; **Fig. 1I**), whereas clusters 6 and 12 (CAFs) significantly interacted with cluster 4 in 50% of samples ($P < 0.01$; **Fig. 1I**). We also found that CAF clusters significantly interacted with cluster 1, a CD4$^+$ T-cell cluster, in line with findings showing that FAP^{high}PDGFRβ^{high} CAFs recruit CD4$^+$CD25$^+$ T cells to the TME

Figure 1.

Positive correlation and spatial interaction between FAP$^+$ CAFs and monocytic myeloid cells in LSCC. **A,** Correlation between FAP expression and CD14 (blue), CD8A (yellow), or CD20 (gray) expression in 501 LSCC patients or 503 LADC patients from TCGA. Spearman correlation was used to determine the correlation coefficient *r*. **B** and **C,** Representative images of the hematoxylin and eosin (H&E) and p63 IHC staining of an LSCC sample. Scale bar, 100 μm. One H&E was done per tumor cross section. **D,** A representative IMC image of an LSCC sample stained with anti-FAP (green), anti–E-cadherin (red), anti-CD14 (magenta), and anti-CD8 (cyan). One 1 mm × 1 mm image was taken from each LSCC sample. Scale bar, 100 μm. **E,** A representative IMC image with a cell segmentation mask as indicated by cell segmentation lines. Scale bar, 100 μm. **F,** E-cadherin$^+$, FAP$^+$, CD14$^+$, or CD8A$^+$ cells were visualized in the t-SNE plot combined from 10 LSCC samples (patient cohort A). **G,** The correlation between percentage of FAP$^+$ in total cells and percentage of CD14$^+$ monocytic myeloid cells from t-SNE plots from each patient. The correlation coefficient was determined by Spearman correlation. **H,** Cell phenotypes from 10 LSCC samples shown in the heat map were determined by normalized median epitope expression of stained markers using antibodies. **I,** All spatial interactions present in 10 LSCC images are represented as a heat map in which the cell type in the row is significantly neighbored (red) or avoided (blue) by the cell type in the column determined in **H**. Significance was determined by a permutation test ($P < 0.01$). Highlighted squares indicate the percentage of images with significant CAF and monocytic myeloid cell interaction.

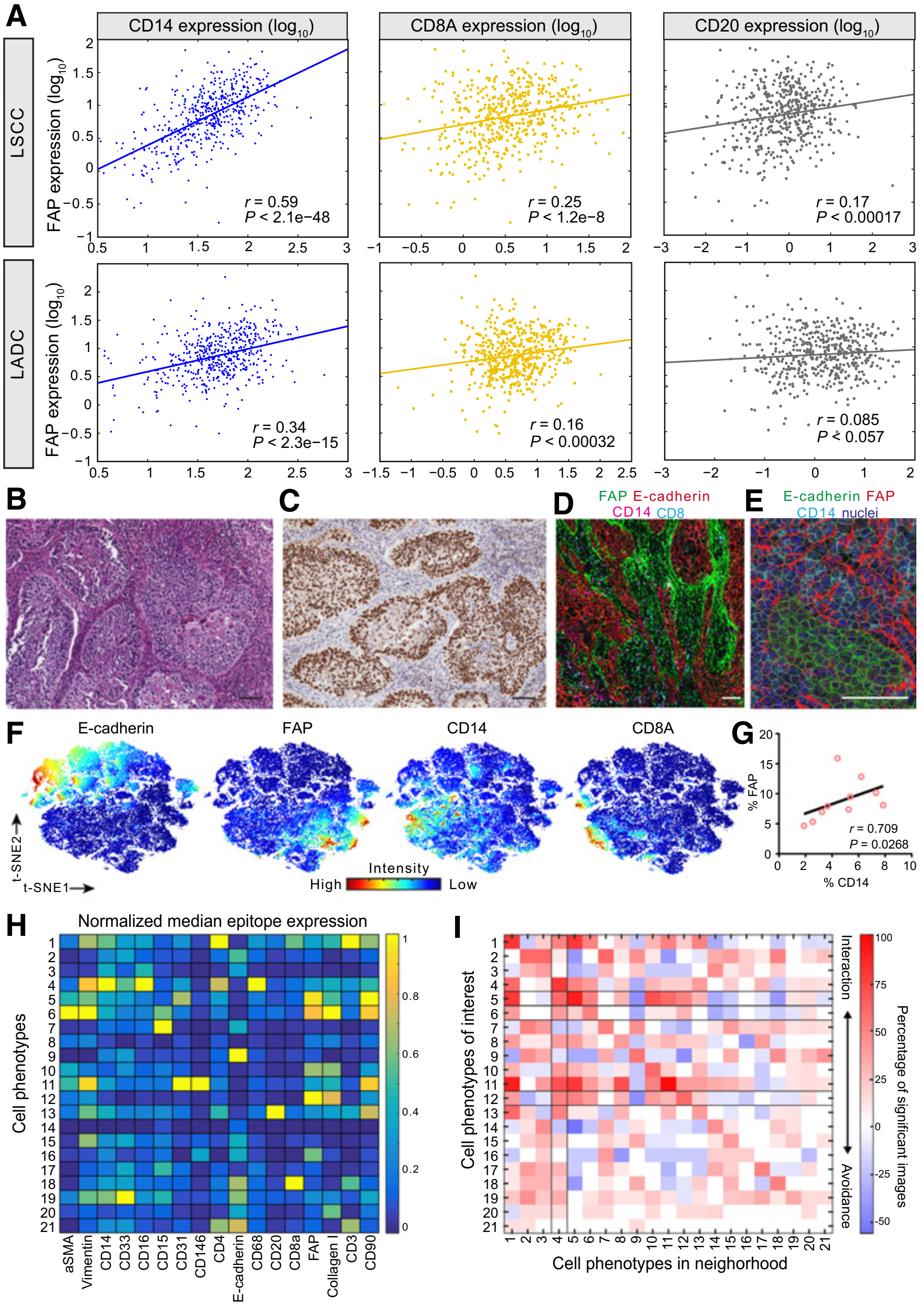

and promote their differentiation to Tregs in breast cancer (9). Collectively, these data revealed a positive correlation between FAP$^+$ fibroblast and monocytic myeloid cell abundances and a spatial interaction of CAFs and monocytic myeloid cells.

Patient-derived CAFs secrete cytokines associated with monocyte recruitment and MDSC expansion

To functionally characterize the association between CAFs and monocytic myeloid cells, we isolated CAFs from three primary LSCCs, herein denoted as CAF_01, 02, and 03 (**Fig. 2A**). Patient-derived CAF identity was phenotypically confirmed by expression of fibroblast-associated markers such as FAP, CD90, and PDGFRβ using flow cytometry (**Fig. 2B**; refs. 23, 24). As expected, expression of these fibroblast markers was not detected in lung squamous tumor cell lines (H520, H2170, and SW900; **Fig. 2C**). We next sought to identify soluble factors produced by LSCC-derived CAFs. To mimic the physiologic microenvironment in which CAFs reside, we cultured CAFs in growth factor–reduced BME in a 3D-transwell system and collected conditioned media. Using a multiplexed immunoassay, we found that all three CAFs consistently secreted readily detectable monocyte- and neutrophil-attracting chemokines, including CCL2, CCL7, CXCL1, CXCL5, and CXCL8, compared with BME alone

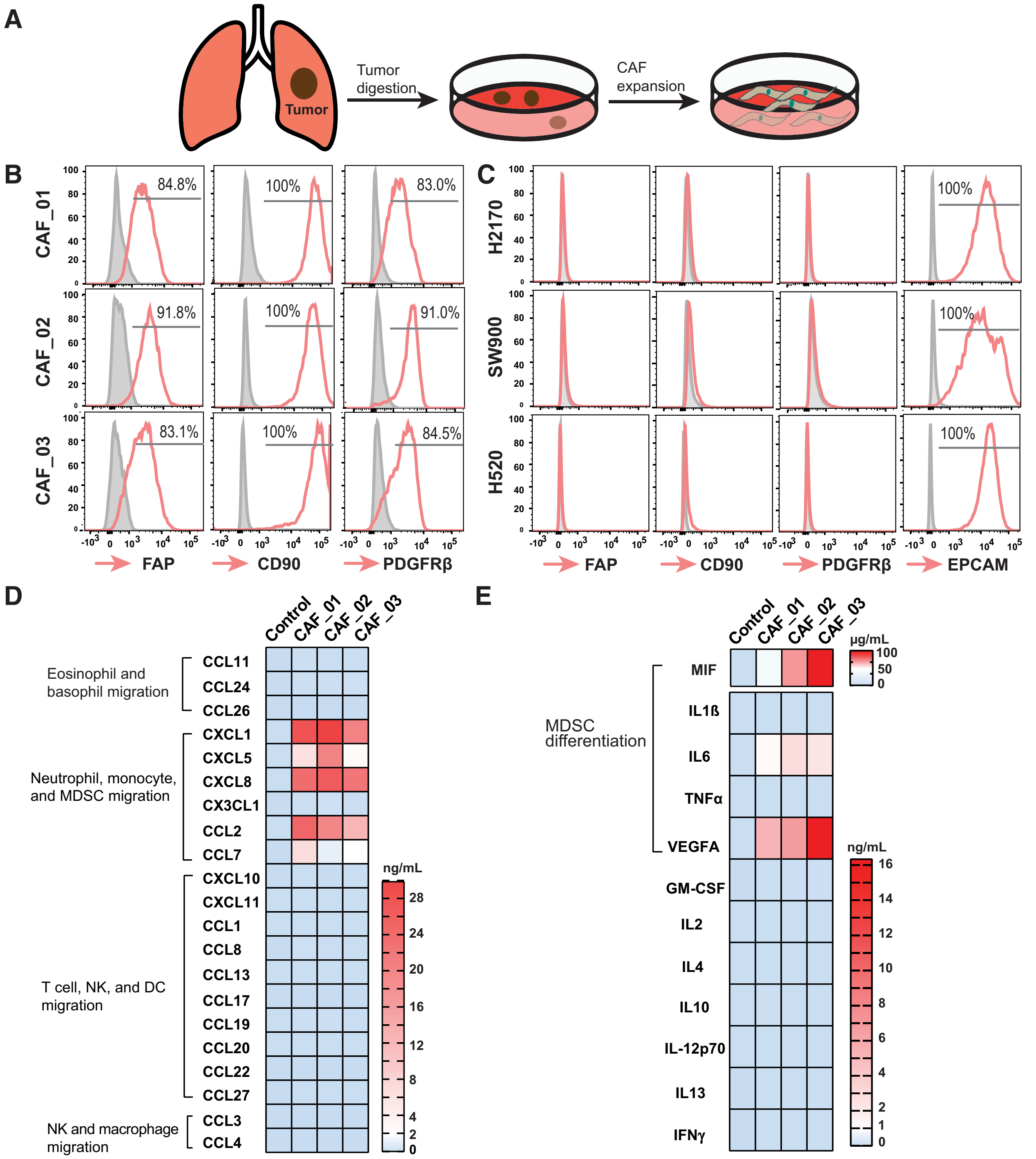

Figure 2.

Chemokine and cytokine profiling of LSCC-derived CAFs from 3 donors. **A,** A schematic illustration of primary CAF isolation and expansion *in vitro*. **B,** Flow cytometry staining of three primary CAFs with anti-FAP, anti-CD90, and anti-PDGFRβ. Gray line, fluorescence minus one (FMO); red line, antibody. Three independent experiments were performed. **C,** Flow cytometry staining of three LSCC tumor cell lines, H2170, SW900, and H520, with anti-FAP, anti-CD90, and anti-PDGFRβ. One independent experiment was performed for each tumor cell line. **D** and **E,** Heat maps showing the concentrations of chemokines or cytokines secreted by primary CAFs from the 3 donors. NK, natural killer.

(**Fig. 2D**). Substantial concentrations of MIF, IL6, and VEGF were also detected in the CAF-conditioned media (**Fig. 2E**). All three factors have been implicated in promoting MDSC differentiation (25, 26).

To further differentiate the contributions of CAFs and tumor cells in modulating monocytic myeloid cells, we analyzed single-cell RNA-sequencing data from a cohort of 5 treatment-naïve NSCLC patients from Lambrechts and colleagues (13). Eight major cell types, including fibroblasts and cancer cells, were identified, and the gene expression of CAF-derived factors in individual cells was evaluated. The transcripts *VEGFA* and *MIF* were ubiquitously expressed by various cell types, whereas *IL6* and *CCL2* transcripts predominantly presented in fibroblasts (Supplementary Fig. S6A and S6B), suggesting that at least in these patients, fibroblasts were likely the primary source of IL6 and CCL2. Due to a limited number of patients, we further analyzed gene expression using a TCGA data set and divided LSCC patients into two groups based on *FAP* expression (FAP$^{\text{low}}$ and FAP$^{\text{high}}$; Supplementary Fig. S6C). Consistent with single-cell RNA-sequencing data, *VEGFA* was comparable between the two groups, whereas the FAP$^{\text{high}}$ group had significantly higher expression of both *IL6* and *CCL2*, suggesting that CAFs and tumor cells may have differential cytokine/chemokine profiles and, thus, disparate capacities to modulate monocytes.

LSCC CAFs promote the migration of CCR2$^+$CD14$^+$monocytes by secreting CCL2

Based on the observed secreted factor profiles, we hypothesized that CAFs may facilitate the recruitment of blood-circulating monocytes to the local TME through secreting specific chemokines. To test this hypothesis, we first examined if conditioned media collected from LSCC-derived CAFs could induce monocyte migration in a chemotaxis assay. CD14$^+$ monocytes isolated from healthy PBMCs were added to the insert well, and conditioned media were applied to the reservoir plate. In comparison with monocytes migrating toward control media, CAF-conditioned media from 3 donors significantly increased monocyte migration by 3- to 6-fold (**Fig. 3A**).

To delineate which chemokines specifically mediate this enhanced cell migration, individual recombinant human proteins CCL2, CCL7, CXCL1, CXCL5, and CXCL8 were added to the media at concentrations detected in the CAF-conditioned media and measured for their ability to attract monocytes. We found that CCL2 significantly increased monocyte migration by 5- or 6-fold with increasing concentrations ($P < 0.01$; **Fig. 3B**).

To understand the role of CCL2 in mediating monocyte migration, we next examined the abundance of chemokine receptors expressed on monocytes. CCR2 is the chemokine receptor for CCL2 and CCL7, whereas CXCR2 serves as the receptor for CXCL1 and CXCL5 (**Fig. 3C**; ref. 27). CXCL8 can bind to two receptors, CXCR1 and CXCR2, with higher binding affinity toward CXCR1 (27). We examined cell-surface expression of the three chemokine receptors in CD14$^+$ monocytes by flow cytometry and found that more than 90% of CD14$^+$ monocytes expressed CCR2 across all donors tested but showed low CXCR1 and CXCR2 expression (**Fig. 3D**). This result is in line with previous findings that CCR2$^+$ cells comprise more than 92% monocytes originating from the bone marrow and spleen and finally circulating into blood (28). To verify low expression of CXCR1 and CXCR2 on monocytes, we used the same antibody clones to stain freshly isolated neutrophils. Consistent with previous studies (27, 29), we detected higher cell-surface expression of CXCR1 and CXCR2 in neutrophils (Supplementary Fig. S7A–S7C), indicating that differential expression of chemokine receptors in monocytes and neutrophils may partially explain the disparate responses to chemokines.

We next interrogated whether blocking the CCL2 receptor CCR2 could mitigate CAF-mediated monocyte chemotaxis. When stimulated with CAF-conditioned media, monocytes exhibited a potent migratory response in the chemotaxis assay. However, the addition of a CCR2 antagonist significantly impaired CAF-mediated chemotaxis of monocytes in a dose-dependent manner (**Fig. 3E** and **F**; ref. 30). Taken together, these results demonstrated that CAFs isolated from LSCC patients could mediate CCR2$^+$ monocyte chemotaxis by secreting CCL2.

LSCC CAFs promote the differentiation of CD14$^+$ monocytes into immunosuppressive MDSCs

To explore the impact of CAFs on monocyte differentiation, we cocultured BME-embedded CAFs with CD14$^+$ monocytes isolated from PBMCs from 3 healthy donors in a transwell system. To compare the phenotype of CAF-educated cells with other monocytic myeloid cell types, we differentiated monocytes into M1 and M2 macrophages, iDCs, and MDSCs according to widely used cytokine treatment methods (25, 31, 32). Because the serum concentration (10% FBS) used to maintain myeloid cells has been well documented to induce the *de novo* acquisition of gene-expression profiles associated with wound healing and cancer in normal fibroblasts, we did not include normal fibroblasts as negative controls. We then examined cell-surface expression of several canonical monocytic myeloid cell markers in each population by flow cytometry. After 7 days of cytokine stimulation, CD14$^+$CD11b$^+$CD33$^+$ monocytes differentiated into various monocytic myeloid populations with differential cell-surface expression of CD14, CD11b, and CD33 (**Fig. 4A**; Supplementary Fig. S8A). Consistent with previous studies demonstrating that GM-CSF and IL4 reduce CD14 expression, we found that iDCs expressed lower CD14 compared with all other cell types (33). CAF-educated cells exhibited significantly lower expression of the DC marker, DC-sign, compared with iDCs and expressed significantly lower CD86 and HLA-DR compared with macrophages, suggesting that CAF-educated monocytes do not differentiate into iDCs or macrophages (**Fig. 4A**). Although CD206 and CD163 are reported to be markers associated with human M2 macrophages (34), cytokine-induced MDSCs and CAF-educated cells had comparable or even higher surface expression of both markers. We also found that CD16 expression was elevated in both cytokine-induced MDSCs and CAF-educated monocytes. It has been suggested that CD16 can serve as a marker for identifying monocytic MDSCs in patients with advanced solid tumors and oligometastases (35). Our data suggest that CAF-educated monocytes phenotypically resemble monocytic MDSCs.

Previous studies have shown that MDSCs can suppress T-cell proliferation in an antigen-independent manner (36, 37). We assessed whether CAF-educated cells could suppress autologous T-cell proliferation in response to polyclonal stimulation. We cocultured CD8$^+$ T cells stimulated with anti-CD3/CD28 beads and other monocytic myeloid populations at a 1:1 or 2:1 effector-to-suppressor ratio. CAF-educated cells suppressed CD8$^+$ T-cell proliferation by more than 90% at the 1:1 (T cell:myeloid cell) ratio and 70% at the 2:1 ratio in all 3 CAF donors (**Fig. 4B**; Supplementary Fig. S8B). CAF-educated cells exhibited more robust activity on a per cell basis than cytokine-derived MDSCs or M2 macrophages in suppressing T-cell proliferation (**Fig. 4B**). CAF-educated cells also significantly inhibited the IFNγ production of CD8$^+$ T cells by 100-fold and 10-fold at the 1:1 and 2:1 (T cell:myeloid cell) ratios, respectively, compared with stimulated T cells alone (**Fig. 4C**). We

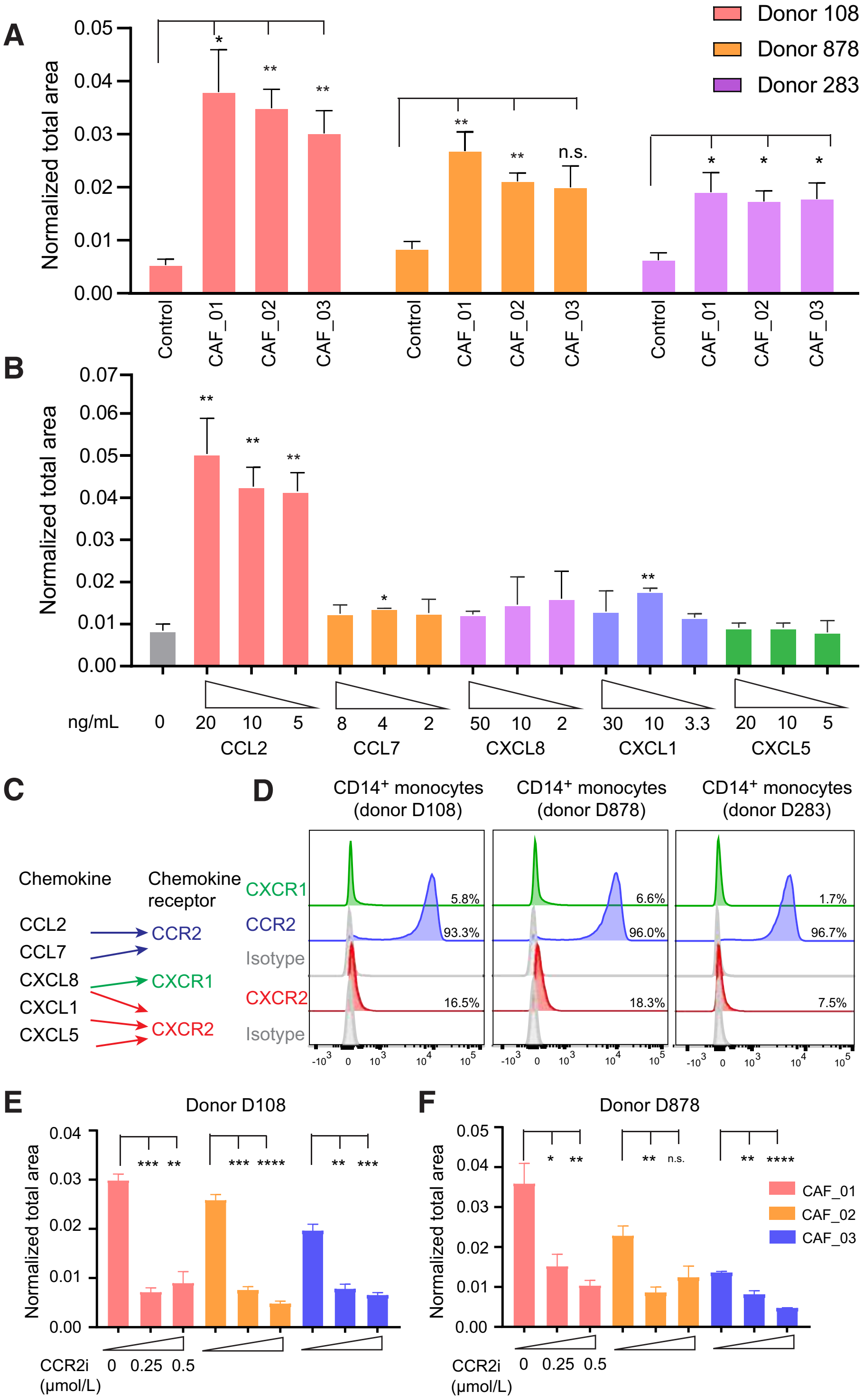

Figure 3.

LSCC-derived CAFs facilitate CD14$^+$CCR2$^+$ monocyte migration through secretion of CCL2. **A,** Directed cell migration reported as normalized total area (lower side cell area normalized to initial upper side cell area). Increased normalized total area indicates enhanced cell migration. CAF-conditioned media from 3 CAF donors were cocultured with CD14$^+$ monocytes isolated from 3 independent PBMC donors (D108, D878, and D283) after 1.5 hours. **B,** The results of monocyte migration toward CCL2-, CCL7-, CXCL8-, CXCL1-, and CXCL5-containing media. **C,** A schematic illustration of chemokine and corresponding chemokine receptors. **D,** Cell-surface expression of CXCR1, CCR2, and CXCR2 in CD14$^+$ monocytes isolated from the 3 PBMC donors. Three independent experiments were performed for each PBMC donor. **E** and **F,** Chemotactic migration of CD14$^+$ monocytes and the effect of treatment with a CCR2 inhibitor (CCR2i) at the indicated concentrations. Bar plots are represented as mean with SEM from three independent experiments, and Student *t* test was used to calculate *P* value. *, $P < 0.05$; **, $P < 0.01$; ***, $P < 0.001$; ****, $P < 0.0001$; n.s., not statistically significant.

did observe around 35% suppressive activity of M1 macrophages at the 1:1 (T cell: myeloid cell) ratio, but not at the 2:1 ratio, likely as a result of excessive myeloid cell numbers present in the culture. Previous studies have shown that MDSCs enhance IDO1 expression, which can deprive local tryptophan in the TME, increase kynurenine, and, thus, inhibit T-cell function (36, 37). Here, we found that treatment with an analogue of the IDO1 inhibitor, epacadostat, significantly reduced the suppressive effect of CAF-induced MDSCs on CD8$^+$ T-cell proliferation by more than 2-fold at 1 and 3 μmol/L concentrations (**Fig. 4D**; ref. 19). Inhibition of IDO1 also increased IFNγ production by T cells (**Fig. 4E**) and reduced kynurenine concentrations in the coculture media, confirming that reversal of T-cell suppression by MDSCs was dependent on IDO1 activity (**Fig. 4F**). We also found that supplying

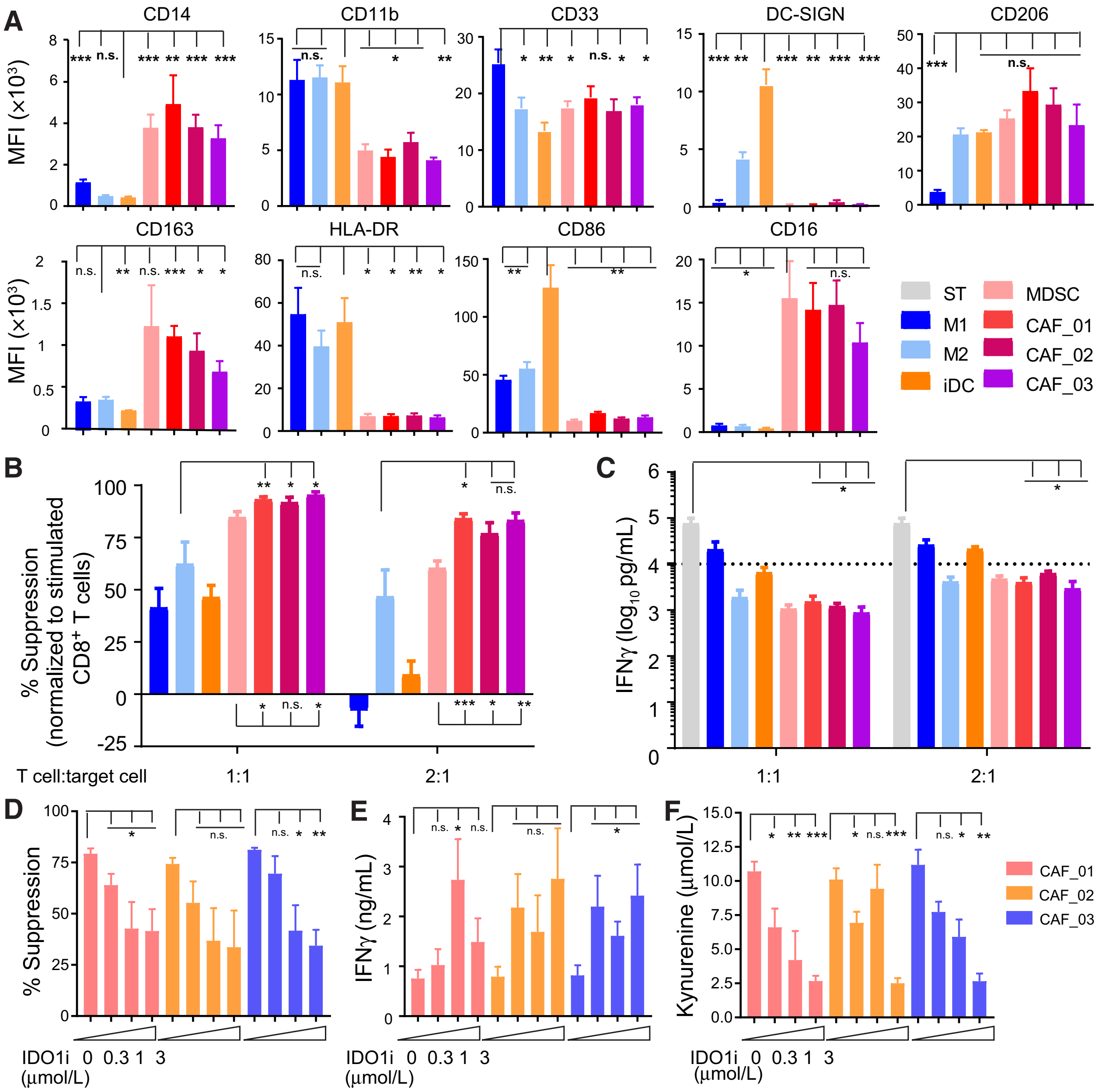

Figure 4.

LSCC-derived CAFs promote monocyte-to-MDSC differentiation. **A,** MFI of cell-surface expression of CD14, CD11b, CD33, DC-SIGN, CD206, CD163, HLA-DR, CD86, and CD16 on M1 and M2 macrophages, iDCs, MDSCs, and CAF-educated cells. ST, stimulated T cells. **B,** Suppression of autologous CD8$^+$ T-cell proliferation by M1 and M2 macrophages, iDCs, MDSCs, and CAF-educated cells. CFSE-labeled CD8$^+$ T cells were stimulated with CD3/CD28 beads and incubated with or without various myeloid cells for 3 days. CFSE fluorescence intensity was assessed by flow cytometry staining. **C,** The concentration of IFNγ was determined in supernatants collected from aforementioned CD8$^+$ T-cell and myeloid cell cocultures. **D,** Suppression of autologous CD8$^+$ T-cell proliferation by CAF-educated cells and the effect of IDO1 inhibitor (IDO1i) treatment at indicated concentrations. Different colors indicate MDSCs induced by different CAF donors. **E** and **F,** IFNγ and kynurenine concentrations in the CD8$^+$ T-cell and myeloid cell cocultures with the IDO1 inhibitor (IDO1i) treatment at indicated concentrations. Different colors indicate MDSCs induced by different CAF donors. All the aforementioned experiments were performed using the 3 PBMC donors (D108, D878, and D283). At least three independent experiments were performed for each donor. Bar plots are represented as mean with SEM, and Student *t* test was used to calculate *P* value. *, $P < 0.05$; **, $P < 0.01$; ***, $P < 0.001$; n.s., not statistically significant.

25 µmol/L tryptophan, comparable with the tryptophan concentration in fresh media, to the culture minimally reversed the suppression of T-cell proliferation (Supplementary Fig. S9A). We detected kynurenine in our system at concentrations less than 15 µmol/L, which impaired T-cell proliferation by ~10%. (Supplementary Fig. S9B). These results indicated that neither tryptophan deprivation nor kynurenine conversion was sufficient to suppress T-cell proliferation in this system.

Proteomic profiling identifies NOX2 in MDSCs to induce immunosuppression by generating ROS

To explore additional mechanisms involved in CAF-induced immunosuppression, we measured the total proteome of immunosuppressive CAF-educated cells and nonimmunosuppressive iDCs to identify differentially expressed proteins using mass spectrometry (**Fig. 5A**). Out of the 3,293 proteins detected, 1,954 proteins consistently detected in all 3 PBMC donors were quantified in the two populations (Supplementary Table S4). The MHC class II family members involved in antigen presentation, such as HLA-DRB1, HLA-DMB, HLA-DQB1, and HLA-DRA, as well as CD74, were enriched in iDCs (**Fig. 5A**). There were 86 proteins significantly enriched in CAF-induced MDSCs compared with iDCs ($P \leq 0.05$, Log_2 fold change $\geq$ 1.0; **Fig. 5A**; Supplementary Table S5). We recapitulated previous findings and identified ~208-fold higher MMP9, an effector molecule of MDSCs to induce angiogenesis and metastasis, expression in CAF-induced MDSCs compared with iDCs (38). CD14 protein expression was also higher in CAF-educated cells compared with iDCs, in line with the cell-surface staining results (**Fig. 4A**). To determine potential biological processes related to immunosuppression of CAF-induced MDSCs, we functionally categorized proteins significantly expressed in either MDSCs or iDCs based on pathway analysis using GeneGo/MetaCore (**Fig. 5B**). Proteins with high expression in iDCs were enriched in DC-related pathways, whereas CCL2-, VEGF-, and MIF-associated pathways were upregulated in CAF-induced MDSCs, a manifestation of the effect of CAF-secreting factors on monocyte differentiation. Oxidative stress (activation of NADPH oxidase pathways) was significantly enriched in CAF-induced MDSCs and has been implicated in dampening T cell–mediated antitumor responses via reactive oxygen species (ROS; ref. 39). We identified four components of the NADPH oxidase-2 (NOX2) enzyme that were enriched in MDSCs compared with iDCs, including the membrane-bound catalytic subunit CYBB (NOX2), CYBA (p22^{phox}), the cytosolic factor NCF2 (p67^{phox}), and the small GRPase RAC2 (40). These cells expressed 10-fold and 2.4-fold higher CYBB and RAC2 than iDCs ($P = 0.011, 0.037$; **Fig. 5C**), whereas CYBA and NCF2 had ~9-fold and 1.9-fold higher expression in MDSCs over iDCs, although the difference was not statistically significant ($P = 0.096, 0.564$; **Fig. 5C**). *CYBB* expression in CAF-induced MDSCs decreased by 4-fold by IL6 neutralization during the coculture, indicating that CAF-secreted IL6 could induce CYBB expression (Supplementary Fig. S10).

To test whether NOX2 expressed in MDSC inhibited CD8^+ T-cell proliferation, we used a selective NOX2 inhibitor, GSK-2795039 (NOX2i), in a T-cell suppression assay (18). Cocultures of CD8^+ T cells and CAF-induced MDSCs were treated with NOX2i for 3 days, and CD8^+ T-cell proliferation was determined by CFSE dilution using flow cytometry. Treatment with NOX2i significantly reduced T-cell suppression (**Fig. 5D**). Because the NOX2 complex is a NADPH oxidase and generates superoxide anions (40, 41), we measured superoxide anions in CAF-induced MDSCs and found reduced levels in cells treated with NOX2i (**Fig. 5E**). This was further validated by using the redox-sensitive fluorescent probe CellROX, which detects a broad range of ROS, including superoxide (**Fig. 5F**). Although we did not detect other NADPH oxidase family members by mass spectrometry, we did observe similar expression of NOX4 protein in both CAF-educated myeloid cells and CAFs by Western blot (Supplementary Fig. S11), indicating that NOX4 in CAF-induced MDSCs may contribute to ROS generation, thus suppressing T-cell proliferation. NOXi inhibits NOX1, NOX2, and NOX4 with a higher potency for NOX1 and NOX4 compared with NOX2 (17). We observed enhanced T-cell proliferation and reduced ROS production with both inhibitors, with a more robust effect using the more selective NOX2 inhibitor, NOX2i (**Fig. 5D**). To confirm that ROS generated by CAF-induced MDSCs played an essential role in restraining T-cell proliferation, we added an ROS scavenger, N-acetylcysteine (NAC), into the coculture system and found that NAC significantly decreased the suppressive effect of CAF-induced MDSCs on T-cell proliferation by 70% at 5 mmol/L (**Fig. 5G**). To further explore clinical relevance of NOX biology, we mined the TCGA data set and identified a significant positive correlation between the expression of CD14 and the two NOX2 subunits, CYBB and CYBA, in LSCC patients (r = 0.86, 0.58; **Fig. 5H** and **I**), supporting our observation that tumor-infiltrating CD14^+ monocytes were likely to adopt an immunosuppressive MDSC phenotype by expressing NOX2 in the TME.

Given that ROS generation is a crucial step in suppressing T-cell proliferation in CAF-induced MDSCs, we examined whether IDO1 also participated in ROS production. This hypothesis was based on observations that IDO pathway metabolites, such as 3-hydroxykynurenine and 3-hydroxyanthranilic acid, may act as oxidative stress generators (42, 43). Consistent with this notion, we stained CAF-induced MDSCs treated with or without the IDO1 inhibitor using CellROX and found that IDO1 inhibition significantly decreased ROS (**Fig. 5J** and **K**).

Discussion

Using over 500 LSCC patient samples, we identified a significant positive correlation between CAFs and monocyte accumulation, which were functionally validated using *ex vivo* cellular systems. We demonstrated that LSCC-derived CAFs could enhance CCR2^+ monocyte migration and induce functional reprogramming of monocytes to immunoinhibitory MDSCs that reduce CD8^+ T-cell proliferation and IFNγ production. We further showed that the interaction between CAFs and monocytes could be disrupted in two ways: (i) targeting CCR2 to abolish the migration of monocytes and (ii) inhibiting IDO1 or NOX2 to hinder ROS generation, thus reversing the immunosuppressive functions of CAF-induced MDSCs (**Fig. 6**).

Previous studies in breast cancer demonstrate that CXCL12 plays a significant role in CAF-induced monocyte chemotaxis (6). Among the various chemokines secreted by LSCC CAFs, we identified CCL2 as the predominant chemoattractant for CCR2^+ monocytes as evidenced by inhibition of monocyte migration upon blockade of the CCL2–CCR2 signaling axis, suggesting the importance of tissue-specific differences in CAF function. Nearly all LSCCs are associated with smoking and characterized by pulmonary fibrosis with upregulation of inflammatory cytokines such as IL6 and CCL2 (44, 45). This may partially explain why we observed a high correlation between CAFs and monocytes in LSCC but not in LADC cases. This specificity is important and implies that CAF-targeting strategies could be optimized for different NSCLC subtypes. CCR2 inhibition in pancreatic cancer patients decreases monocytic MDSCs in phase Ib trials (NCT02345408), and these patients respond better to the CCR2 antagonist, CCX872, in combination with FOLFIRINOX or chemotherapy compared with chemotherapy alone (46, 47). As such, we speculate that pharmacologic CCR2 inhibition may be one strategy to prevent early CAF-monocyte cross-talk in LSCC, thus reducing subsequent MDSC differentiation.

We demonstrated that LSCC CAFs polarized monocytes to MDSCs that exert an immunosuppressive phenotype by antagonizing

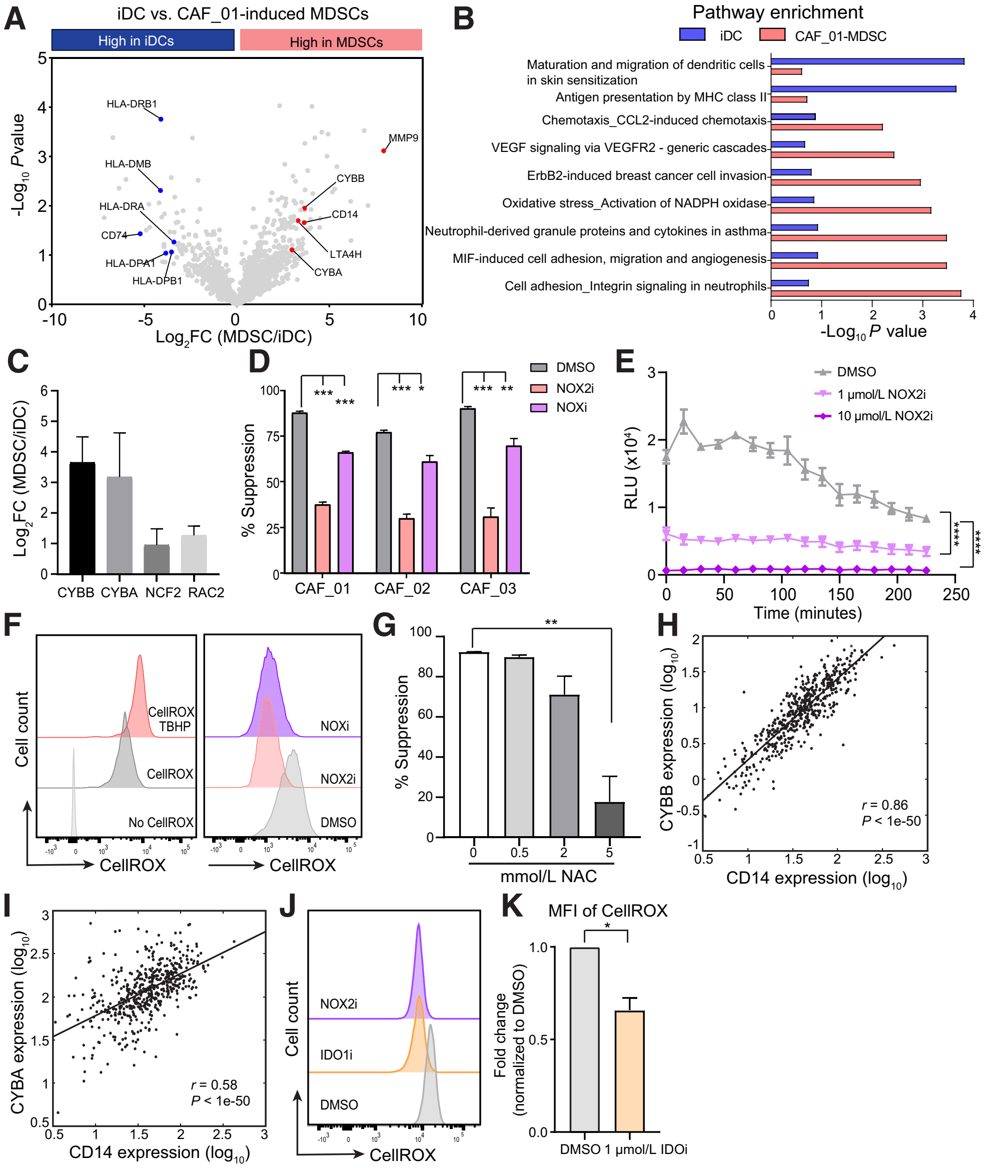

Figure 5.

Proteomics analysis to identify novel proteins that mediate the immunosuppressive function of CAF-induced MDSCs. **A,** Differentially expressed proteins between CAF_01-educated MDSCs and iDCs identified by mass spectrometry. Blue dots highlight some significant differentially expressed proteins in iDCs ($P \leq 0.05$, Log2 fold change ≥1.0), whereas red dots show several significant differentially expressed proteins in CAF_01-induced MDSCs identified in the screen. The experiment was performed by using the 3 PBMC donors, and Student *t* test was used to calculate *P* value. **B,** Pathway analysis of proteins enriched in either iDCs or CAF_01-induced MDSCs. Blue bar, iDC-enriched pathways; red bar, CAF_01-induced MDSC–enriched pathways. **C,** Log2 fold change of CAF_01-induced MDSCs over iDCs of CYBB, CYBA, NCF2, and RAC2 by proteomic profiling. Bar plots are represented as mean with SEM. **D,** Either 10 μmol/L NOX2 inhibitor or 10 μmol/L NOX inhibitor was incubated with CFSE-labeled CD8^+ T cells in the presence of CAF-induced MDSCs for 3 days (2 CD8^+ T-cell:1 MDSCs), and suppression of CD8^+ T-cell proliferation was assessed by CFSE dilution. Bar plots are represented as mean with SEM from at least three independent experiments using the PBMC donor D878, and Student *t* test was used to calculate *P* value. **E,** The production of superoxide anions of CAF_01-induced MDSCs treated with DMSO (control) or NOX2i at the indicated concentrations. RLU, raw luminescence unit. The method is based on the oxidation of luminol by superoxide anions resulting in the formation of chemiluminescence light. Results are represented as mean with SEM from three independent experiments using the PBMC donor D878. Two-way ANOVA was used to calculate *P* value. **F,** Representative histogram showing the fluorescence intensity of CellROX in control MDSCs, MDSCs treated with a ROS inducer, TBHP (left), and NOX inhibitor–treated CAF_01-induced MDSCs for 1 day (right). Three independent experiments were performed using the PBMC donor D878. **G,** The antioxidant NAC at different concentrations was incubated with CFSE-labeled CD8^+ T cells and CAF_01-induced MDSCs (2 CD8^+ T-cell:1 MDSCs). Suppression of T-cell proliferation was assessed by CFSE dilution. Bar plots are represented as mean with SEM from three independent experiments using the PBMC donor D878, and Student *t* test was used to calculate *P* value. **H** and **I,** Correlation between CD14 expression and CYBB or CYBA expression in 501 LSCC patients from TCGA. Spearman correlation was used to determine the correlation coefficient *r* and *P* value. **J,** Representative histograms showing the fluorescence intensity of CellROX in CAF_01-induced MDSCs treated with DMSO or inhibitors at indicated concentrations for 1 day. **K,** Quantification of fold changes of CellROX MFI in the IDO1 inhibitor (IDO1i)–treated group compared with the DMSO group. Bar plots are represented as mean with SEM from three independent experiments using the PBMC donor D878. Paired *t* test was used to calculate *P* value for this graph. *, $P < 0.05$; **, $P < 0.01$; ***, $P < 0.001$; ****, $P < 0.0001$; n.s., not statistically significant. Log2FC, Log2 fold change; NOXi, NOX inhibitor; NOX2i, NOX2 inhibitor.

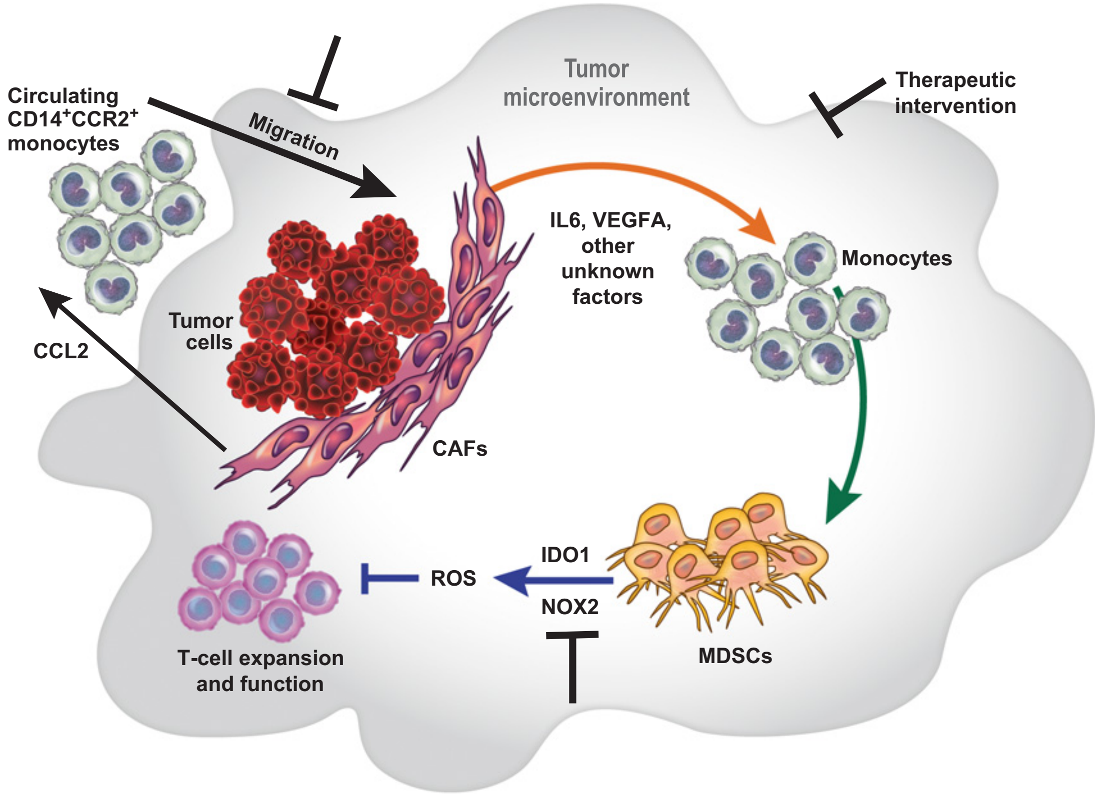

Figure 6.

The schematic representation of the study. CCL2-secreting CAFs facilitate the migration of blood-circulating CD14$^+$CCR2$^+$ monocytes to the local TME. CAFs directly interact with monocytes and promote monocyte-to-MDSC differentiation. CAF-induced MDSCs further inhibit CD8$^+$ T-cell proliferation by upregulating the expression of NOX2 and IDO1 to generate excessive ROS. Targeting CCR2, IDO1, and NOX2 can reverse the malignant interaction between CAFs and monocytic myeloid cells.

antitumor T-cell immunity. The tryptophan catabolic enzyme indoleamine 2,3-dioxygenase-1 (IDO1) has garnered much attention in driving cancer immunosuppression, rooted to its function in inflammatory programming and MDSC support (48). Previous studies showed that Ido1$^{-/-}$ mice resist the outgrowth of lung tumors, and MDSCs obtained from tumor-bearing animals do not impair T-cell function (49). Similarly, we demonstrated that inhibition of IDO1 in LSCC CAF-induced MDSCs with an epacadostat analogue partially restored T-cell proliferation. However, IDO1 inhibition in combination with anti–PD-1 has seen limited success in phase III clinical trials for melanoma patients (50). Our results suggest that using kynurenine to extrapolate IDO1 inhibitor efficacy in clinical trials is insufficient. One study shows that kynurenine concentrations in lung cancer patient blood range from 1.02 μmol/L to 2.29 μmol/L (51). Although it is difficult to deduce accurate kynurenine concentrations in the TME, at least a 50- to 100-fold increase in kynurenine may be required to impact T-cell proliferation. Thus, the immunosuppressive mechanism underlying the IDO pathway likely converges on other signaling pathways, such as ROS generation in MDSCs, to dampen antitumor T-cell immune responses.

Unbiased proteome measurements enabled the identification of the protein complex, NOX2, that mediated the immunosuppressive role of MDSCs in impairing T-cell function. The NOX2 enzyme is a multicomponent enzymatic complex containing two membrane proteins, CYBB and CYBA, and several cytosolic elements, p47^{phox}, p67^{phox}, p40^{phox}, and small G proteins (40). This oxidase is a myeloid-specific member of the NADPH oxidase family whose main function is to produce ROS (40). Excessive ROS have been shown to induce T-cell apoptosis and downregulate the expression of the TCR ζ-chain (38, 39). Our findings showed that NOX2 inhibition reduced ROS production in CAF-educated MDSCs and, thus, restored T-cell proliferation. Consistent with our studies, Corzo and colleagues report that Gr-1$^+$CD11b$^+$ MDSCs isolated from tumor-bearing mice produce significantly higher ROS and have enhanced CYBB expression compared with immature myeloid cells from tumor-free mice (40).

Taken together, our study delineated the interplay of the stromal (CAFs) and immune cell (monocytic MDSCs and T cells) compartments in lung tumors and provides conceptual insights into how CAFs may shape an immunosuppressive TME. Our study also suggests therapeutic targets, such as CCR2 and NOX, to disrupt these interactions to augment antitumor immune function. We showed that blocking either IDO1 or NADPH oxidase activity could lead to ROS reduction and restoration of T-cell proliferation. Thus, efficiently scavenging excessive ROS to maintain the redox balance in the TME may improve T-cell responses and warrants further investigation. As with all *ex vivo* systems, prospective preclinical *in vivo* experiments will be needed to substantiate the hypothesis of our work.

Disclosure of Potential Conflicts of Interest

H. Xiang is a senior scientist at Merck & Co., Inc. C.P. Ramil is a postdoctoral research fellow at Merck & Co., Inc. J. Hai is a senior scientist at Merck & Co., Inc. C. Zhang is a scientist at and has ownership interest (including patents) in Merck & Co., Inc. P. Georgiev is a senior scientist at Merck & Co., Inc. X.S. Song is a senior scientist at Merck & Co., Inc. J.R. Miller is a director at Merck & Co., Inc. L.Y. Moy is Director, Pharmacology, at Merck & Co., Inc. P.E. Brandish is Director, Research Science, at, reports receiving a commercial research grant from, and has ownership interest (including patents) in Merck & Co., Inc. No potential conflicts of interest were disclosed by the other authors.

Authors' Contributions

Conception and design: H. Xiang, J. Hai, P.E. Brandish

Development of methodology: H. Xiang, C.P. Ramil, H. Wang, R. Afshar, P. Georgiev, X.S. Song, D. Sun, Y. Jia, A. Chi, P.E. Brandish

Acquisition of data (provided animals, acquired and managed patients, provided facilities, etc.): H. Xiang, C.P. Ramil, J. Hai, A.A. Watkins, P. Georgiev, X.S. Song, P.J. Curran, M. Cheng, J.R. Miller, D. Sun, L.Y. Moy

Analysis and interpretation of data (e.g., statistical analysis, biostatistics, computational analysis): H. Xiang, C.P. Ramil, J. Hai, C. Zhang, H. Wang, A.A. Watkins, M.A. Sze, X.S. Song, P.J. Curran, M. Cheng, A. Loboda

Writing, review, and/or revision of the manuscript: H. Xiang, C.P. Ramil, J. Hai, H. Wang, A.A. Watkins, R. Afshar, P. Georgiev, M.A. Sze, X.S. Song, M. Cheng, D. Sun, L.Y. Moy, A. Chi, P.E. Brandish

Study supervision: L.Y. Moy, A. Chi, P.E. Brandish

Other (developed and validated an LC-MS methodology to enable the detection of kynurenine, labeled kynurenine, tryptophan, and labeled tryptophan): P.J. Curran

Acknowledgments

We would like to thank Dr. Denis Schapiro for histoCAT training and Ying Huo for operating Hyperion Imaging System. We acknowledge Doug Linn for IMC experimental design, Latika Singh for suggestions on MDSC differentiation, Benjamin Ruprecht for input on proteomics data analysis and interpretation, and Amy D. DeCastro for providing reagents. The authors acknowledge support from the Merck Research Laboratories Postdoctoral Research Program.

The costs of publication of this article were defrayed in part by the payment of page charges. This article must therefore be hereby marked *advertisement* in accordance with 18 U.S.C. Section 1734 solely to indicate this fact.

Received July 3, 2019; revised November 14, 2019; accepted February 13, 2020; published first February 19, 2020.

References

1. Doroshow DB, Sanmamed MF, Hastings K, Politi K, Rimm DL, Chen L, et al. Immunotherapy in non-small cell lung cancer: facts and hopes. Clin Cancer Res 2019;25:4592–602.
2. Kalluri R. The biology and function of fibroblasts in cancer. Nat Rev Cancer 2016;16:582–98.
3. LeBleu VS, Kalluri R. A peek into cancer-associated fibroblasts: origins, functions and translational impact. Dis Model Mech 2018;11. pii: dmm029447.
4. Loeffler M, Kruger JA, Niethammer AG, Reisfeld RA. Targeting tumor-associated fibroblasts improves cancer chemotherapy by increasing intratumoral drug uptake. J Clin Invest 2006;116:1955–62.
5. Valkenburg KC, de Groot AE, Pienta KJ. Targeting the tumour stroma to improve cancer therapy. Nat Rev Clin Oncol 2018;15:366–81.
6. Gok Yavuz B, Gunaydin G, Gedik ME, Kosemehmetoglu K, Karakoc D, Ozgur F, et al. Cancer associated fibroblasts sculpt tumour microenvironment by recruiting monocytes and inducing immunosuppressive PD-1(+) TAMs. Sci Rep 2019;9:3172.
7. Mariathasan S, Turley SJ, Nickles D, Castiglioni A, Yuen K, Wang Y, et al. TGFbeta attenuates tumour response to PD-L1 blockade by contributing to exclusion of T cells. Nature 2018;554:544–8.
8. Cristescu R, Mogg R, Ayers M, Albright A, Murphy E, Yearley J, et al. Pan-tumor genomic biomarkers for PD-1 checkpoint blockade-based immunotherapy. Science 2018;362. pii: eaar3593.
9. Costa A, Kieffer Y, Scholer-Dahirel A, Pelon F, Bourachot B, Cardon M, et al. Fibroblast heterogeneity and immunosuppressive environment in human breast cancer. Cancer Cell 2018;33:463–79.e10.
10. Cho H, Seo Y, Loke KM, Kim SW, Oh SM, Kim JH, et al. Cancer-stimulated CAFs enhance monocyte differentiation and protumoral TAM activation via IL6 and GM-CSF secretion. Clin Cancer Res 2018;24:5407–21.
11. Mace TA, Ameen Z, Collins A, Wojcik S, Mair M, Young GS, et al. Pancreatic cancer-associated stellate cells promote differentiation of myeloid-derived suppressor cells in a STAT3-dependent manner. Cancer Res 2013;73:3007–18.
12. Cancer Genome Atlas Research N, Weinstein JN, Collisson EA, Mills GB, Shaw KR, Ozenberger BA, et al. The cancer genome atlas pan-cancer analysis project. Nat Genet 2013;45:1113–20.
13. Lambrechts D, Wauters E, Boeckx B, Aibar S, Nittner D, Burton O, et al. Phenotype molding of stromal cells in the lung tumor microenvironment. Nat Med 2018;24:1277–89.
14. Schapiro D, Jackson HW, Raghuraman S, Fischer JR, Zanotelli VRT, Schulz D, et al. histoCAT: analysis of cell phenotypes and interactions in multiplex image cytometry data. Nat Methods 2017;14:873–6.
15. Jones TR, Kang IH, Wheeler DB, Lindquist RA, Papallo A, Sabatini DM, et al. CellProfiler analyst: data exploration and analysis software for complex image-based screens. BMC Bioinformatics 2008;9:482.
16. Amir el AD, Davis KL, Tadmor MD, Simonds EF, Levine JH, Bendall SC, et al. viSNE enables visualization of high dimensional single-cell data and reveals phenotypic heterogeneity of leukemia. Nat Biotechnol 2013;31:545–52.
17. Schildknecht S, Weber A, Gerding HR, Pape R, Robotta M, Drescher M, et al. The NOX1/4 inhibitor GKT136901 as selective and direct scavenger of peroxynitrite. Curr Med Chem 2014;21:365–76.
18. Hirano K, Chen WS, Chueng AL, Dunne AA, Seredenina T, Filippova A, et al. Discovery of GSK2795039, a novel small molecule NADPH oxidase 2 inhibitor. Antioxid Redox Signal 2015;23:358–74.
19. Zhang H, Liu K, Pu Q, Achab A, Ardolino MJ, Cheng M, et al. Discovery of amino-cyclobutarene-derived indoleamine-2,3-dioxygenase 1 (IDO1) inhibitors for cancer immunotherapy. ACS Med Chem Lett 2019;10:1530–6.
20. Zaragoza B, Chen X, Oppenheim JJ, Baeyens A, Gregoire S, Chader D, et al. Suppressive activity of human regulatory T cells is maintained in the presence of TNF. Nat Med 2016;22:16–7.
21. Brennen WN, Isaacs JT, Denmeade SR. Rationale behind targeting fibroblast activation protein-expressing carcinoma-associated fibroblasts as a novel chemotherapeutic strategy. Mol Cancer Ther 2012;11:257–66.
22. Levine JH, Simonds EF, Bendall SC, Davis KL, Amir el AD, Tadmor MD, et al. Data-driven phenotypic dissection of AML reveals progenitor-like cells that correlate with prognosis. Cell 2015;162:184–97.
23. Ohlund D, Elyada E, Tuveson D. Fibroblast heterogeneity in the cancer wound. J Exp Med 2014;211:1503–23.
24. Puram SV, Tirosh I, Parikh AS, Patel AP, Yizhak K, Gillespie S, et al. Single-cell transcriptomic analysis of primary and metastatic tumor ecosystems in head and neck cancer. Cell 2017;171:1611–24.e24.
25. Lechner MG, Megiel C, Russell SM, Bingham B, Arger N, Woo T, et al. Functional characterization of human Cd33$^+$ and Cd11b$^+$ myeloid-derived suppressor cell subsets induced from peripheral blood mononuclear cells co-cultured with a diverse set of human tumor cell lines. J Transl Med 2011;9:90.
26. Simpson KD, Cross JV. MIF: metastasis/MDSC-inducing factor? Oncoimmunology 2013;2:e23337.
27. Griffith JW, Sokol CL, Luster AD. Chemokines and chemokine receptors: positioning cells for host defense and immunity. Annu Rev Immunol 2014;32:659–702.
28. Franca CN, Izar MCO, Hortencio MNS, do Amaral JB, Ferreira CES, Tuleta ID, et al. Monocyte subtypes and the CCR2 chemokine receptor in cardiovascular disease. Clin Sci (Lond) 2017;131:1215–24.
29. Petering H, Gotze O, Kimmig D, Smolarski R, Kapp A, Elsner J. The biologic role of interleukin-8: functional analysis and expression of CXCR1 and CXCR2 on human eosinophils. Blood 1999;93:694–702.

30. Cherney RJ, Mo R, Meyer DT, Nelson DJ, Lo YC, Yang G, et al. Discovery of disubstituted cyclohexanes as a new class of CC chemokine receptor 2 antagonists. J Med Chem 2008;51:721–4.
31. Chapuis F, Rosenzwajg M, Yagello M, Ekman M, Biberfeld P, Gluckman JC. Differentiation of human dendritic cells from monocytes in vitro. Eur J Immunol 1997;27:431–41.
32. Rey-Giraud F, Hafner M, Ries CH. In vitro generation of monocyte-derived macrophages under serum-free conditions improves their tumor promoting functions. PLoS One 2012;7:e42656.
33. Ruppert J, Schutt C, Ostermeier D, Peters JH. Down-regulation and release of CD14 on human monocytes by IL-4 depends on the presence of serum or GM-CSF. Adv Exp Med Biol 1993;329:281–6.
34. Biswas SK, Mantovani A. Macrophage plasticity and interaction with lymphocyte subsets: cancer as a paradigm. Nat Immunol 2010;11:889–96.
35. Chen HM, Ma G, Gildener-Leapman N, Eisenstein S, Coakley BA, Ozao J, et al. Myeloid-derived suppressor cells as an immune parameter in patients with concurrent sunitinib and stereotactic body radiotherapy. Clin Cancer Res 2015; 21:4073–85.
36. Nagaraj S, Youn JI, Gabrilovich DI. Reciprocal relationship between myeloid-derived suppressor cells and T cells. J Immunol 2013;191:17–23.
37. Marvel D, Gabrilovich DI. Myeloid-derived suppressor cells in the tumor microenvironment: expect the unexpected. J Clin Invest 2015;125:3356–64.
38. Fleming V, Hu X, Weber R, Nagibin V, Groth C, Altevogt P, et al. Targeting myeloid-derived suppressor cells to bypass tumor-induced immunosuppression. Front Immunol 2018;9:398.
39. Chen X, Song M, Zhang B, Zhang Y. Reactive oxygen species regulate T cell immune response in the tumor microenvironment. Oxid Med Cell Longev 2016; 2016:1580967.
40. Corzo CA, Cotter MJ, Cheng P, Cheng F, Kusmartsev S, Sotomayor E, et al. Mechanism regulating reactive oxygen species in tumor-induced myeloid-derived suppressor cells. J Immunol 2009;182:5693–701.
41. Aydin E, Johansson J, Nazir FH, Hellstrand K, Martner A. Role of NOX2-derived reactive oxygen species in NK cell-mediated control of murine melanoma metastasis. Cancer Immunol Res 2017;5:804–11.
42. Okuda S, Nishiyama N, Saito H, Katsuki H. 3-Hydroxykynurenine, an endogenous oxidative stress generator, causes neuronal cell death with apoptotic features and region selectivity. J Neurochem 1998;70: 299–307.
43. Goldstein LE, Leopold MC, Huang X, Atwood CS, Saunders AJ, Hartshorn M, et al. 3-Hydroxykynurenine and 3-hydroxyanthranilic acid generate hydrogen peroxide and promote alpha-crystallin cross-linking by metal ion reduction. Biochemistry 2000;39:7266–75.
44. Papiris SA, Tomos IP, Karakatsani A, Spathis A, Korbila I, Analitis A, et al. High levels of IL-6 and IL-8 characterize early-on idiopathic pulmonary fibrosis acute exacerbations. Cytokine 2018;102:168–72.
45. Kolahian S, Fernandez IE, Eickelberg O, Hartl D. Immune mechanisms in pulmonary fibrosis. Am J Respir Cell Mol Biol 2016;55:309–22.
46. Linehan D, Noel MS, Hezel AF, Wang-Gillam A, Eskens F, Sleijfer S, et al. Overall survival in a trial of orally administered CCR2 inhibitor CCX872 in locally advanced/metastatic pancreatic cancer: correlation with blood monocyte counts. J Clin Oncol 36, 2018 (suppl 5S; abstr 92).
47. Noel MS, Hezel AF, Linehan D, Wang-Gillam A, Eskens F, Sleijfer S. Orally administered CCR2 selective inhibitor CCX872-b clinical trial in pancreatic cancer. J Clin Oncol 2017;35:276.
48. Prendergast GC, Malachowski WJ, Mondal A, Scherle P, Muller AJ. Indoleamine 2,3-dioxygenase and its therapeutic inhibition in cancer. Int Rev Cell Mol Biol 2018;336:175–203.
49. Smith C, Chang MY, Parker KH, Beury DW, DuHadaway JB, Flick HE, et al. IDO is a nodal pathogenic driver of lung cancer and metastasis development. Cancer Discov 2012;2:722–35.
50. Labadie BW, Bao R, Luke JJ. Reimagining IDO pathway inhibition in cancer immunotherapy via downstream focus on the tryptophan-kynurenine-aryl hydrocarbon axis. Clin Cancer Res 2019;25:1462–71.
51. Chuang SC, Fanidi A, Ueland PM, Relton C, Midttun O, Vollset SE, et al. Circulating biomarkers of tryptophan and the kynurenine pathway and lung cancer risk. Cancer Epidemiol Biomarkers Prev 2014;23:461–8.